Case Studies in Construction Materials 24 (2026) e05978

Contents lists available at ScienceDirect

Case Studies in Construction Materials

journal homepage: www.elsevier.com/locate/cscm

Under-calcination thermal reactivation of hydrated cement pastes and construction and demolition waste: A comparison of different commercial products

A. Bisciotti [a,*], S. Castellini [b], A. Neri [b], P. Šajna [c], S. Dolenec [c,d], A. Balbo [e], G. Cruciani [a]

[a] University of Ferrara, Department of Physic and Earth Sciences, Ferrara, Italy
[b] Colacem Spa, Laboratorio Tecnologico Centrale, Località Ghigiano, Italy
[c] Slovenian National Building and Civil Engineering Institute - ZAG, Ljubljana, Slovenia
[d] University fof Ljubljana, Faculty of Natural Sciences and Engineering, Department of Geology, Ljubljana, Slovenia
[e] University of Ferrara, Department of Engineering, Corrosion and Metallurgy Study Centre "Aldo Daccò", Ferrara, Italy

ARTICLE INFO

Keywords:
Secondary SCMs
Thermal reactivation
Hydrated cement
Clinker minerals

ABSTRACT

This study explores the properties of supplementary cementitious materials (SCMs) obtained from the under-calcining thermal reactivation of construction and demolition waste fines (CDW) and of pure hydrated cement pastes (HCPs) derived from different commercial cements (CEM I, CEM II, CEM III, and CEM IV, classified according to EN 197–1). Samples were thermally treated at 350 °C (low-energy activation) and 600 °C (high-reactivity optimization) to increase pozzolanic and/or hydraulic behavior without inducing CO_2 release from calcination. Phase transformations were analyzed by X-ray Powder Diffraction with Rietveld refinement, thermal behavior by TGA/DTA, and morphological evolution by SEM, while reactivity and hydration kinetics were assessed using isothermal calorimetry. Results indicate pronounced differences in thermal response among the HCPs and CDW, governed by their specific phase assemblages and initial SCM content (limestone, slag, and pozzolans). At the selected under-calcining high-reactivity temperature (600 °C), γ-C_2S formation is favored. Thermal reactivation of slag-rich cement (CEM III) yielded the most reactive circular SCM, combining both high hydraulic (260 J/g - EN 196–11) and pozzolanic (329 J/g - ASTM C1897–20) performances with reduced carbon impacts.

1. Introduction

Driven by the need to reduce its environmental impact, the cement industry is actively seeking Supplementary Cementitious Materials (SCMs) that can partially replace clinker in Portland cement manufacture (M. C. G. [1]). Their incorporation in blended cement not only cuts down the CO_2 footprint of the material but often provides enhanced durability and strength at later ages [2]. In recent years, the dominant SCMs have been industrial by-products such as fly ash, ground granulated blast furnace slag (GGBFS), and silica fume (M. [3]). These materials result from high-emission industries like coal and steel, which might be limited in the future if net-zero emission pathways are followed [4]. Therefore, alternative SCMs are increasingly sought to prevent future shortages, reduce

* Corresponding author.
E-mail address: bscndr@unife.it (A. Bisciotti).

https://doi.org/10.1016/j.cscm.2026.e05978
Received 17 November 2025; Received in revised form 24 February 2026; Accepted 13 March 2026
Available online 14 March 2026

transportation distances, and minimize the exploitation of additional mineral deposits [5,6]. To meet the sustainable development goals, the building sector shall also include the efficient recycling of construction and demolition waste (CDW) in a circular economy [7]. The estimated production of such waste in Europe is 800 Mt/year, accounting for over 50% of total solid waste generated [8]. Most of this waste is currently recycled for subbase and base in road construction, whereas the use in concrete or blended cements is still limited [9]. Previous studies have investigated the use of CDW in the production of recycled aggregates and filler with SCM potential demonstrating promising results [10–12].

When directly produced from crushed concrete the CDW is typically composed of inert natural aggregates (NAs) and of hydrated cement paste (HCP) adhering to the surface. The amount of HCP may vary considerably according to crushing methods, grain size, ageing, type and initial strength grade of the cement embedded [13,14]. In general, the amount of HCP increases with the decrease of CDW grain size, which is known to have detrimental effects in recycled aggregates [15]. Excluding the use as raw materials in the cement kiln, other potential applications are carbon capture and storage (CCS) or the production of SCMs [16–18]. When tested as SCMs, the CDW fine fractions originally display a low reactivity, therefore necessitating further processing either mechanical, chemical, thermal, or combined [19]. The main concept involves isolating the HCP from waste concrete, grinding it into a fine powder, and then heating it at high temperatures to restore its reactivity (D. [20]). Nevertheless, CDW is typically enriched in calcite, resulting either from the inert NAs fraction or from the HCP, which limits thermal processing above decarboxylation temperature [21,22].

Similarly to clinker cement production, when powdered HCP is heated, dicalcium silicate (C_2S) is the first to form through solid-state reactions below 1300 °C, above this temperature also tricalcium silicate phase (C_3S) might form [23]. However, unlike clinker raw meals, where the β polymorph of C_2S is the first to form, in HCP it mainly results in the formation of (*alpha*) α-C_2S [24,25]. More specifically, the alpha prime-high (α'_H-C_2S) orthorhombic polymorph has been previously identified [26]. The (*beta*) β-C_2S is only formed at temperatures above 800 °C due to polymorphic transformation of α-C_2S to β-C_2S [26]. The α-C_2S is a more reactive polymorph than the β-C_2S [27] and is apparently produced after the process of dehydration and depolymerization of the calcium silicate hydrates (C-S-H) at around 600°C where also portlandite dihydroxylation occurs [28]. The (*gamma)* γ-C_2S polymorph, characterized by zero hydraulic activity, is not commonly reported in thermal reactivated HCPs, and seems to form between 500 and 700°C [29]. Lastly in the range of 750–1000°C, in the presence of calcite, lime is formed, and CO_2 is again emitted [30]. The tricalcium aluminate (C_3A) and ferrite (C_4AF) can form above 850°C but is usually a later product, assuming that enough Al_2O_3 is present [31].

The process previously described involves the thermal reactivation of Ordinary Portland Cement (OPC, classified as CEM I according to EN 197–1), which might serve as reference HCP. However, blended cement such as CEM II, CEM III, and CEM IV (as defined by EN 197–1) are increasingly being adopted in construction and are therefore found as HCPs in CDW. Most of the available literature focuses on the thermal reactivation of CDW fines produced from CEM I, while how these different HCPs behave remains largely unexplored, and which type has the greatest potential for thermal reactivation in terms of their hydraulic and pozzolanic properties, key characteristics of each SCM [32]. These fine additives are not inert fillers; rather, they actively participate in the hydration reactions, and potentially also in the thermal reactivation process, although through different mechanisms. The presence of GGBFS and pozzolans (in CEM III and IV, respectively) contributes additional aluminum and silicon, which might modify the composition of C-S-H products into calcium aluminate hydrate (C-A-H) and calcium(alumina)silicate hydrate C-(A-)-S-H gel [33,34]. In contrast, limestone additions in CEM II could influence the Ca/Si and Al/Si ratios of the resulting hydration products, that might alter the chemical composition, structure, and morphology of the C-S-H gels (J. [35]).

Thus, to improve understanding of this process with a case study, the most common commercially available cement products have been collected, transformed into HCP, thermally reactivated and then tested for their potential as SCMs, both as pozzolanic and hydraulic materials. As a reference of the real-world impact of the HCP content, a concrete derived CDW sample obtained from a recycling plant, was subjected to the same processes. Most previous studies identified the temperature range between 600 and 800°C as the most effective [21]; however, only a few have explored low-temperature and short-duration treatments aimed at reducing energy demand and CO_2 emissions ([36,37]; D. [20]). Therefore, two under-calcining temperatures were chosen: T1 at 350 °C and T2 at 600 °C. The T1 focused on activating the SCMs pozzolanic potential from dehydration and amorphization with minimal energy consumption and CO_2 emissions, whilst the latter, T2, aimed at maximizing the binding and hydraulic properties from C_2S crystallization, while still avoiding calcite dissociation and high energy consumption [21,28]. The decarboxylation becomes significant already at 500–600°C if a sufficient low partial pressure of CO_2 is maintained or if the calcite is mixed with quartz or clays that can react with the calcium oxide [38].

To monitor the evolution of HCPs from ambient temperature through T1 (350°C) and T2 (600°C), the samples were analyzed using X-ray Powder Diffraction (XRPD) combined with Rietveld refinement. Quantitative phase analysis (QPA) was performed on the crystalline fraction, and by incorporating an internal standard (corundum) the amorphous content was also quantified. In addition to capturing snapshots at specific temperatures, thermal transformations and phase changes across the entire heating range (0–900 °C) were investigated using thermogravimetric analysis (TGA) and differential thermal analysis (DTA). The sample's microstructure morphology is then captured through scanning electron microscopy (SEM). The reactivity of the samples, before and after thermal treatment, was assessed from multiple perspectives, with particular focus on reaction kinetics and energy release determined by isothermal calorimetry using two complementary methods. The first approach, by Isothermal Conduction Calorimetry (ICC) EN 196–11, examines hydration behavior over time by recording the heat flow generated from the dissolution of SCM minerals in water [39,40]. The second approach follows the more recent ASTM C1897–20 (R^3 test), which evaluates the chemical reactivity of SCMs, both pozzolanic and hydraulic, in simulated cement pore solution pastes ([41]; X. [42]). Eventually, this case study offers an in-depth analysis whether different types of blended cements and CDW can be effectively repurposed as SCMs at the end of their life cycle, supporting the transition toward sustainable, and performance-oriented materials.

2. Materials

2.1. Hydrated Cement Pastes

HCPs were prepared in the laboratory using a water-to-cement ratio of 0.5, following the standard 3-minute mixing procedure specified in EN 196–3. The fresh pastes were cast into molds (60 × 40 × 40 mm^3) for 24 h. After demolding, the specimens were maintained under laboratory conditions (20 ± 2 °C with a relative humidity not lower than 50%) for a total of 27 days. At 28 days of hydration, the HCP samples were crushed below 2 cm using a jaw crusher, then ground with a disc mill for 4 min (Fig. 1). The final products (< 90 μm) were collected by sieving. The samples obtained are listed in Table 1.

Thermal treatment was performed in a muffle furnace, with heating from room temperature (T amb.) at 10 °C/min to the target temperatures of 350 °C (T1) and 600 °C (T2), each held for 2 h. Most previous studies adopted an annealing time of 2–3 h [21], sufficient to achieve complete dehydration at temperatures between 500 – 800°C. After treatment, the powders were left to cool to room temperature inside the furnace. Each HCP sample was therefore divided and labeled into T1 and T2 samples based on the thermal treatment conducted. The chemical composition of the samples is provided in Table 2.

2.2. Construction waste fines

The starting CDW contains more than 90% of structural concrete (> 40 MPa, 28 days compressional strength) obtained from the demolition of an industrial pavement. Sample materials were collected from the stock in accordance with standard EN 932–1. Following the sampling procedure, the CDW is homogenized and reduced in the laboratory using a quartering method (EN 932–2). Fines CDW, enriched in HCP, have been obtained by intensive shredding through ball-milling to achieve an extra-fines fraction. A fraction with a finesse below 90 μm was again collected (Fig. 1). The same thermal processing has been conducted on this material and labeled as CDW (25°C), CDW-T1 (350°C) and CDW-T2 (600°C). The chemical composition of the samples determined by wavelength-dispersive X-ray fluorescence spectrometry (XRF) on pressed powder pellets using an ARL Advant-XP+ spectrometer, is provided in Table 2.

A schematic representation of the sample preparation is provided in Fig. 2.

3. Methods

3.1. X-ray Powder Diffraction

X-ray Powder Diffraction (XRPD) analyses were performed using a Bruker D8 Advance Da Vinci diffractometer equipped with a standard Cu X-ray tube (λ = 1.5406 Å) and a Ti filter for Kα radiation. Measurements were collected at room temperature over the 2θ range of 3–90°, employing a Bruker cylindrical specimen holder in PMMA for powder samples. The instrument operated with variable slits ensuring a fixed sample illumination of 15 mm. Data were acquired in 0.02° steps using a Position Sensitive Detector (PSD). Phase identification was accomplished using the DIFFRACT.EVA suite, utilizing the Powder Diffraction File (PDF-2) database maintained by the International Centre for Diffraction Data (ICDD) along with the Inorganic Crystal Structure Database (ICSD). Accurate quantitative phase analysis (QPA) was conducted through the Rietveld profile fitting method applied to the X-ray diffraction patterns, employing the Bruker TOPAS 5.0 software. The QPA results from Rietveld calculations are obtained by convolution-based profile fitting, which combines instrument-related contributions (e.g., beam shape) and sample-related contributions (e.g., crystallite size and microstrain) to generate realistic diffraction profiles. Additional constraints are applied to unit cell dimensions and peak shape parameters to ensure refinement stability [43]. In addition to crystalline phases, the amorphous content was quantified using 15% corundum (Al_2O_3) as an internal standard. This approach allows the indirect estimation of the approximate content of amorphous and semi-amorphous phases,

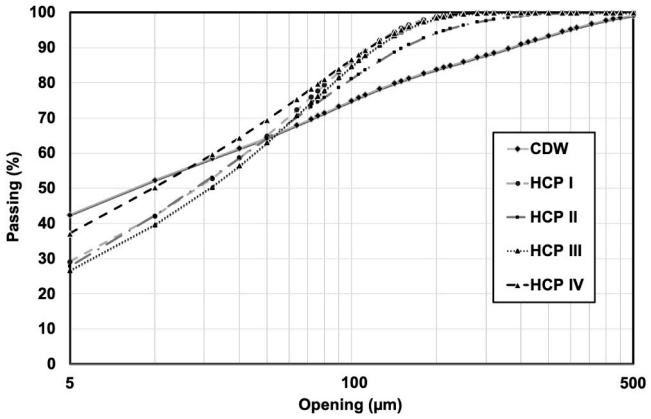

Fig. 1. Grain size distribution of the samples after 4 min of disc milling.

Table 1
Materials composition of hydrated cement pastes (HCPs) used in this study.

Samples	*CEM Type (EN 197–1)*	*Clinker content (wt%)*	*SCMs content (wt%)*	*SCMs type*	*w/c*	*Class of strength*
HCP I	CEM I	95–100	-	-	0.5	52.5 R
HCP II	CEM II/A-LL	80–94	6–20	Limestone	0.5	42.5 N
HCP III	CEM III/B	20–34	66–80	GGBFS	0.5	42.5 N
HCP IV	CEM IV/A -P	65–89	11–35	Natural Pozzolans	0.5	42.5 N

Table 2
XRF (wt%) chemical composition of the samples under investigation.

Samples	SiO_2	Al_2O_3	CaO	Fe_2O_3	MgO	P_2O_5	TiO_2	MnO	Na_2O	K_2O	LOI
CDW	10.05	1.84	50.17	1.26	0.65	0.06	0.09	0.07	0.15	0.38	35.27
HCP I	17.59	2.73	45.49	2.07	0.95	0.08	0.14	0.10	0.59	1.17	29.09
HCP II	15.30	3.61	55.60	2.70	1.22	0.06	0.13	0.13	0.29	0.52	20.42
HCP III	25.55	4.37	37.59	1.21	3.56	0.08	0.22	0.07	0.47	0.40	26.47
HCP IV	25.68	5.00	34.24	2.28	1.08	0.10	0.20	0.06	1.04	2.04	28.27

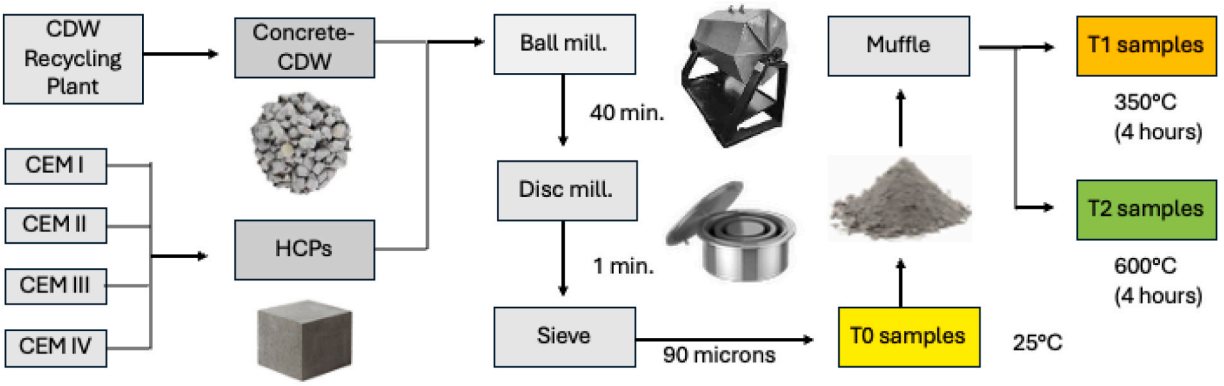

Fig. 2. Schematic representation of the sample's preparation.

such as C-S-H, C-A-H, and C-S(-A)-H, whose broad humps typically overlap with the background and underlie the bases of more crystalline peaks. All peaks, with their specific intensity and crystal sizes derived from the full-width half maximum (FWHM), are modeled together with a background polynomial function refined using 15 coefficients. Preferred orientation effects are addressed by applying texture models such as March-Dollase and spherical harmonics for clay minerals. The quality of each refinement was evaluated using the residual weighted profile (Rwp) value and by visual inspection of the difference between observed and calculated profiles on the same scale. The achieved Rwp values, all below the target threshold of 10.0, are reported in Supplementary Table I. The results reflect single observations per condition, precluding statistical analysis of variability. Quantitative comparisons should therefore be interpreted cautiously.

3.2. Thermogravimetric analysis

Thermogravimetric and Differential Thermal Analyses (TGA-DTA) were performed using a Netzsch-Gerätebau GmbH STA 409 PC Luxx Simultaneous Thermal Analyzer (Netzsch, Germany). Approximately 30 mg of each powdered sample was analyzed, together with corundum (Al_2O_3) used as a reference in the same amount. Measurements were carried out in the temperature range 20–900 °C at a heating rate of 10 K/min, under an oxygen atmosphere. The results were processed and interpreted using the Netzsch Proteus software.

3.3. Reactivity

The isothermal calorimetry has been conducted following the ASTM C1897–20 standard: Standard Test Methods for Measuring the Reactivity of SCMs by Isothermal Calorimetry and Bound Water Measure. The measurements were conducted using a TAM Air 8 calorimeter (TA Instruments). The ASTM C1897–20 test, is a calorimetry test that simulates cementitious pore solution by mixing SCMs with calcium hydroxide (CH), calcium carbonate ($CaCO_3$), potassium sulfate (K_2SO_4), and potassium hydroxide (KOH), and curing the paste at 40 °C for 3 and 7 days. The method does not distinguish between hydraulic and pozzolanic reactivity but rather provides an overall reactivity measure. One measurement per sample was carried out. The cumulative heat of hydration was calculated using the

Eq. (1):

$$\mathbf{HSCM} = \frac{H}{(mp * 0,101)} \quad (1)$$

Where **H** represents the cumulative heat release measured at 3 and 7 days, **mp** is the mass of the paste (15 g in this case), and **0.101** is the mass fraction of each sample within the paste.

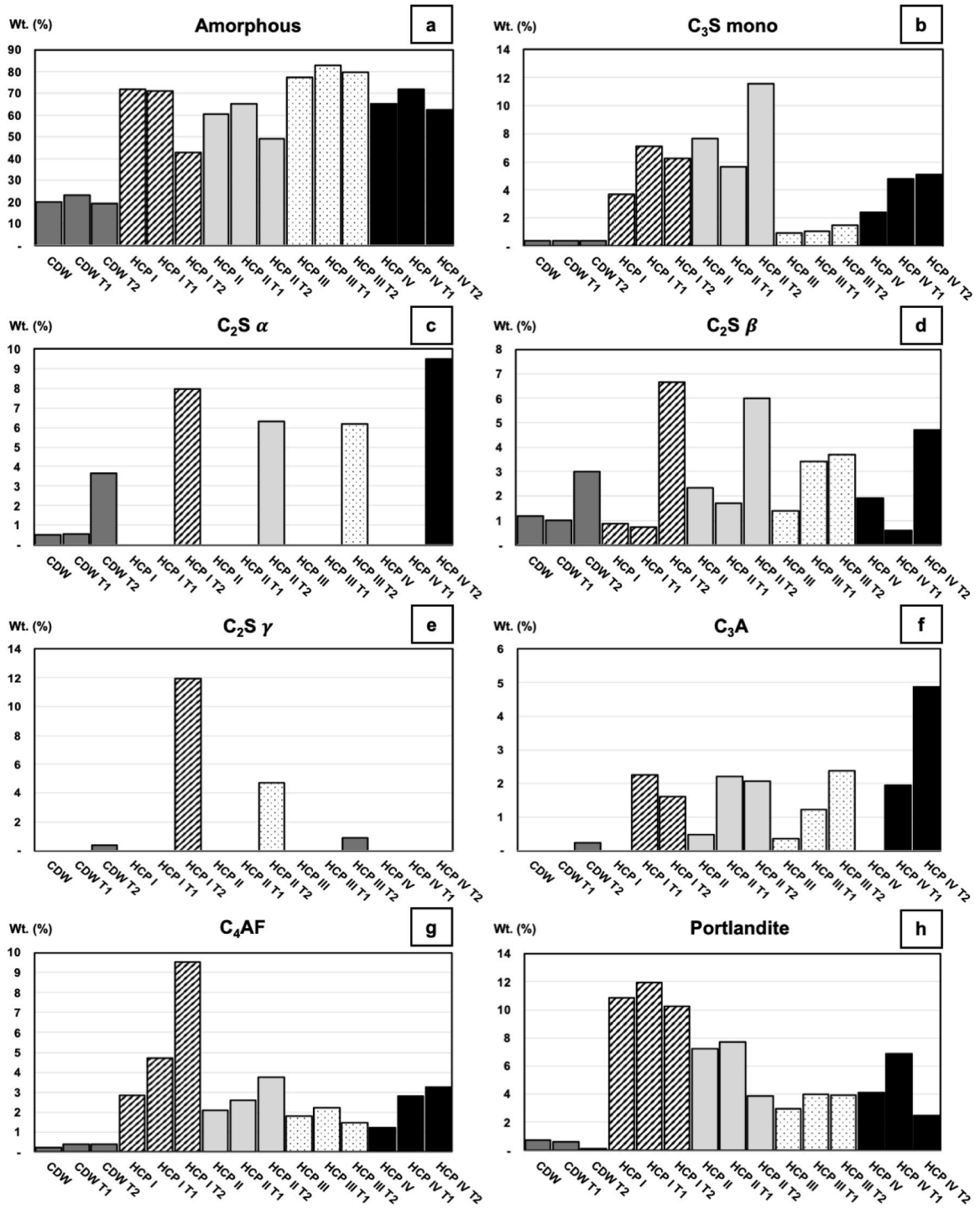

Fig. 3. Bar plots with the QPA Rietveld wt. (%) mineralogical assemblage following XRPD analyses.

3.4. Heat of hydration

Isothermal calorimetry can be used as both a qualitative and quantitative method to study the kinetics of cement hydration. The reactivity of cement samples was assessed following the EN 196–11 standard: Methods of testing cement – Part 11: Heat of hydration - Isothermal Conduction Calorimetry method. To this aim, 10 g of the binder (sample) and 10 g of distilled water were placed into separate, airtight, containers, while 6.05 g of distilled water was placed in glass ampoules to serve as the reference material. Sample preparation was carried out in accordance with EN 196–11. Following preparation, 10 g of the cement paste (w/c =1) was transferred into glass ampoules, which were simultaneously inserted into the calorimeter together with reference ampoules containing distilled water. Single measurement was carried out per sample. The measurements were conducted using a TAM Air 8 calorimeter (TA Instruments). For this purpose, the investigated samples were analyzed together with a reference 52.5 N OPC (Fig. 14), with the standard method EN 196–11, previously described. The cumulative heat of hydration was calculated using the Eq. (2):

$$\mathbf{HNOR} = \frac{H}{m} \tag{2}$$

Where H represents the cumulative heat release measured at 3 and 7 days and m the mass of the binder (5 g in this case).

3.5. Scanning electron microscopy

The HCP and CDW samples were characterized for powder morphology, composition, and internal phase distribution using Scanning Electron Microscopy (SEM) coupled with Energy Dispersive Spectroscopy detector (EDS). Sample preparation for morphological and compositional analysis involved depositing the ground powders onto stubs covered with an adhesive layer. For the internal composition and phase distribution characterization, cross-sections of the powders were prepared. Each powder was cold-mounted in a mold using an epoxy resin (Struers Epofix). Once the resin cured, the resulting samples were polished using abrasive papers and diamond suspensions down to a 1μm. The analyses were conducted using a ZEISS EVO MA 15 electron microscope equipped with a LaB6 source (Carl Zeiss AG, Oberkochen, Germany) and an EDS detector, type X-Max 50 N (Oxford Instruments Abingdon, Oxfordshire, UK). SEM analyses were performed using an electron accelerating voltage (EHT) of 20 kV in low vacuum mode, at a SEM chamber pressure of 70 Pa, to avoid charging artifacts. More than 500 K counts were collected for each EDS spectrum and element distribution maps were acquired with more than 30 M Cts. The collected spectra were processed with Oxford Instruments Aztec 3.3 software.

4. Results and discussion

4.1. X-ray Powder Diffraction and Rietveld QPA

4.1.1. Mineralogical composition and transformation of HCPs

The XRPD patterns measured, the Rietveld profiles calculated, together with the QPA values obtained are provided in Figure I and Table I of Supplementary Materials. For the HCPs samples the crystalline phases mainly represent the traditional clinker minerals such as C_3S, C_2S, C_3A and C_4AF, which remained as unreacted products after the hydraulic reaction ends [23]. Nevertheless, within the low-crystalline to amorphous spectrum are also identified and quantified the hydration products such as ettringite (AFt), portlandite (CH) and the hydrated calcium aluminates (AFm) based on the hydrocalumite-like structure [44]. When it comes to the C-S-H, C-A-H, and C-S(-A)-H, these hydraulic products are not directly measured, but only through the amorphous total content a general estimation is conducted [33,45]. At T amb. (25°C), the HCPs are mainly composed of an amorphous fraction, ranging from 48% to 77%, which in the case of HCP I shall mainly represent the C-S-H content. HCP III exhibits an even higher amorphous content due to the intrinsic glassy nature of the GGBFS addition [46]. In contrast, HCP II and IV present lower amorphous fractions, consistent with the predominance of crystalline minerals of limestone and natural pozzolans [47].When heating to T1 (350°C) (Fig. 3**a**), the amorphous content in HCP I shows only a slight reduction (~1%), whereas all blended HCPs record an increase of about 5–6%. Beyond uncertainties in the measurements, this increase is likely attributable to the transformation of crystalline domains into X-ray–amorphous phases following the loss of structural water and the consequent collapse into a more disordered structure [48]. Among these, AFt and AFm phases (including monosulfate and carboaluminate forms) are present in small amounts at T amb. (0.5–3.5%) but completely disappear by 350 °C. For the C–S–H structure and its variants, which are inherently poorly crystalline, previous studies indicate that around 100 °C water molecules dissociate in order to preserve the hydroxyl population [49]. At approximately 350 °C, dehydroxylation of C–S–H is known to induce more significant structural variability and disorder, including interlayer collapse, merging of calcium layers, and changes in silicate morphology, a process that might explain the 5–6% wt. increase reported in the amorphous content at T1 ([50]; Y. [51]). The CH, follows a different trend (Fig. 3**b**). Its content increases by a few percentage points in all the samples from T amb. to T1, then sharply decreases at T2 but without fully disappearing. The literature reports portlandite dehydroxylation between 450 and 500 °C [52]. The persistence of CH peaks at T2 has been previously explained by partial and rapid rehydration of free lime (CaO) during cooling and storage [53]. However, it could alternatively be explained by incomplete dehydroxylation of portlandite (e.g., due to insufficient temperature, residence time, or local kinetic constraints) or by phase protection effects, where CH domains are shielded by surrounding C–S–H or densified microstructures, delaying or preventing full decomposition [29,54].

Following T2 (600 °C), the amorphous content sharply declines in all HCPs as a result of complete C–S–H dehydration and the crystallization of new clinker phases, a process known to initiate at this temperature [55]. In HCP I the drop is ~30% whereas in the other blended HCPs the reduction is less pronounced, between 3% and 16%, beyond uncertainty estimation. Considering the variation of the amorphous content between T2 and T amb. and comparing it with the wt% of total C_2S formed, it suggests that the reduction of the first is associated with the formation of the latter.

Regarding C_2S polymorph crystallization, the α-form is absent at both T amb. and T1, confirming that this phase does not persist under ambient conditions after hydration occurred. At T2, however, crystallization of α'_H-C_2S (ICSD: 82997, Fig. 4) begins, reaching values above 5% in all samples (Fig. 3**c**). The highest content is observed in HCP IV (9.5%), followed by HCP I (7.9%), while HCP II and III show similar values (both ≈6%); however, these relatively small differences between samples are particularly sensitive to measurement uncertainties. The structure of α'H-C_2S is known to be stabilized by sodium oxide (Na_2O), potassium oxide (K_2O), boron (using sodium tetraborate decahydrate - $Na_2B_4O_7{\cdot}10\ H_2O$), or oxidizing Sulphur atmosphere (SO_4^{2-}) at 1350–1400°C [56–58]. The stabilization is known to result from ionic substitutions for calcium and silicon constituents [59]. Therefore, the higher content of the α'_H polymorph in HCP IV and HCP I might not be random. Indeed, these two have the highest content of alkali ($Na_2O + K_2O$) among the HCPs (Table 2) with 3.08% and 1.76% respectively.

The β-C_2S polymorph is already present at T amb. and T1 (Fig. 3**d**), indicating its persistence after hydration due to its low reactivity compared to the α-form. At T2, β-C_2S increases in all the samples, with the highest content in HCP I (6.67%), followed by HCP II (5.99%), HCP IV (4.69%), and HCP III (3.70%). The β-C_2S is deemed as a distorted α' structure formed during cooling stage at 680–630°C [61,62]. However, based on the present research this temperature range might be lower in the case of HCPs thermal activation [63,64].

The nonhydraulic γ-C_2S polymorph is also found within the samples at T2, whereas at T amb. and T1 this inert phase is completely absent (Fig. 3**e**). This is the dominant C_2S phase at 550 °C, which is close to the T2 value, and crystallizes during equilibrium cooling from the conversion of the α phase [29]. Indeed, at T2 it is detected in HCP I (11.94%) and HCP II (4.69%), while remaining negligible in HCP III and IV; however, in these latter samples its characteristic peaks may be obscured by the high amorphous background (Fig. 6). Rapid cooling or chemical impurity substituents hinder the transformation of α-C_2S to γ- C_2S [61]. Since the first was kept identical for all the samples, the latter condition should have prevail.

The monoclinic M3 form described by De La Torre et al. [65] is adopted as crystalline information file structure (CIF). Any C_3S detected in the samples at the different temperatures is attributed to residual anhydrous constituents of the original cement paste remaining after hydration (1–3%), as seen in HCP I. Higher C_3S values in HCP II (Fig. 3**f**) suggest reduced hydration efficiency, possibly due to fine clays or porous limestone particles hindering reaction despite identical w/c ratios. At T1 and T2, variations in C_3S content mainly reflect dehydration bias: water loss and recrystallization sharpen diffraction peaks. This effect is also observed for anhydrous C_3A and C_4AF (Table I in Supplementary Materials).

Fig. 5 presents the Rietveld-calculated profiles in HCP samples after T2, with the measured pattern shown in red at the top and the individual contributions of the various C_2S polymorphs stacked underneath. The main crystalline peaks are identified and labeled on top of the figure. HCP I shows the sharpest XRPD peaks, consistent with its lowest amorphous fraction (42.76%) and highest cumulative C_2S content (26.57%), indicating extensive crystallization. The calculated profiles for α-, β-, and γ-C_2S closely match the measured reflections. HCP II exhibits a comparable pattern but with slightly higher amorphous content and lower C_2S, reflected in broader background signals and weaker peak intensities. In contrast, the blended HCP III and IV display a markedly different pattern, dominated by a higher amorphous contribution with a peak near 28° (2θ) from vitreous silico-aluminates (GGBFS or natural pozzolan). Nevertheless, C_2S polymorph peaks remain mostly traceable, and the calculated profiles accommodate peak broadening. Although such conditions can affect accuracy in the absence of an internal standard, reliable quantification is ensured here by the addition of corundum.

4.1.2. *Mineralogical composition and transformation of CDW*

The complete XRPD-QPA results for the CDW samples are reported in Table I of the Supplementary Materials. Based on the QPA data, adopting the method described by [15], the amount of leftover cement paste (LCP, also referred to as HCP) is estimated. This approach provides a measure of the LCP and the NAs content from the weight percentages (wt%) of specific mineral groups obtained from the QPA. More in detail, the NAs fraction is determined from common rock-forming minerals such as calcite, quartz, feldspars, and micas. The LCP fraction, on the other hand, is quantified from the anhydrous clinker phases (C_3S, C_2S, C_3A, C_4AF), hydration

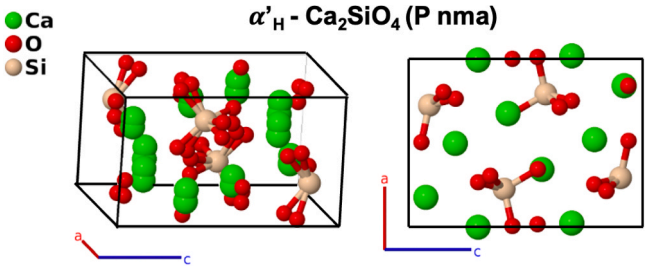

Fig. 4. Crystal structure of α'_H-C_2S (ICSD: 82997) structure data from [60].

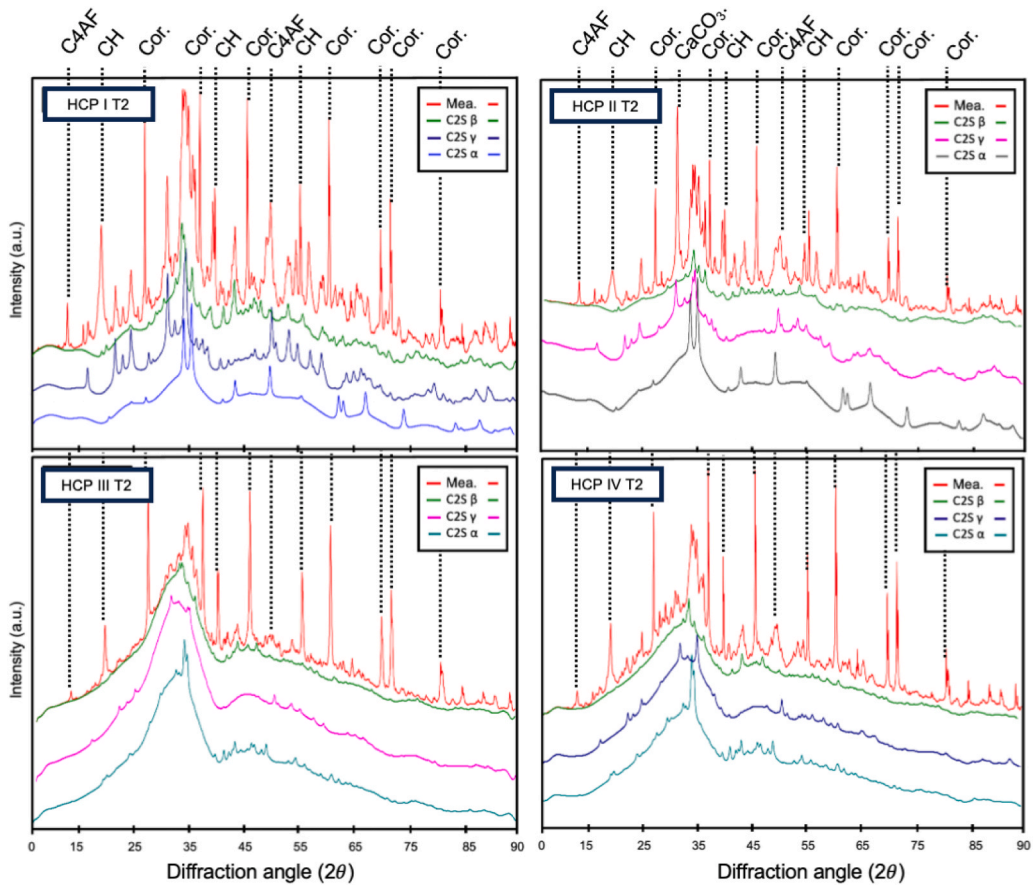

Fig. 5. XRPD pattern of HCPs after thermal activation at T2 (600°C), measured pattern in red (Mes.) and calculated profiles for C_2S- α, C_2S- β, C2S-γ. Other crystalline peaks identified are C4AF, CH, Cor. = corundum (internal standard), $CaCO_3$.

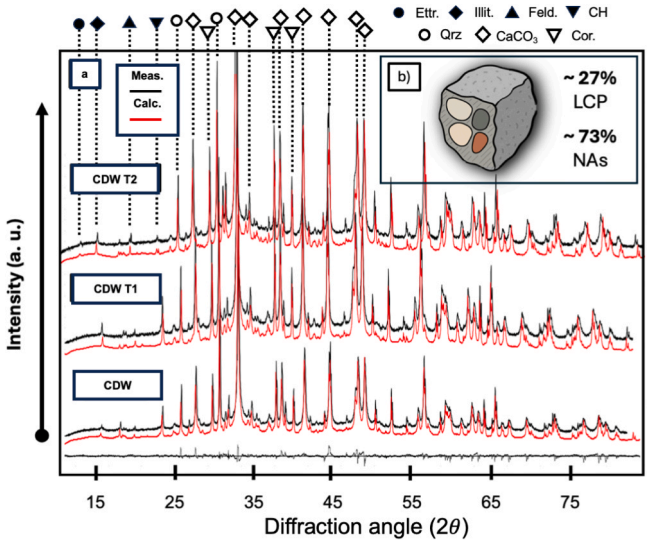

Fig. 6. XRPD pattern measured and calculated from QPA at T amb., T1 and T2 for the CDW (a), volume reconstruction of the leftover cement pastes vs. natural aggregate fraction.

products (CH, AFt and AFm phases, C–S–H), and carbonated cement, calculated from calcite polymorphs and by using a bi-modal crystallite distribution (Fig. 6**a**). The LCP content was found to be approximately 27% in the analyzed CDW sample (Fig. 6**b**), corresponding to an average of 73% embedded NAs. These values are consistent with most findings reported in the literature [66–69]. In this perspective the CDW, after the comminution conduct, and based on its composition, can be eventually associated to a hypothetical HCP II sample where the clinker content is low to 25% and with a 75% SCM content from limestone (Table 1).

Based on the QPA results (Fig. 7, and Supplementary Table I), at T amb., the CDW contains 19.87% amorphous phase, which can largely be attributed to the C–S–H component. The main C_2S polymorphs identified are α (0.5%) and β (1.2%), while CH and C_3S are both below 1%. Other hydration products, such as AFt and AFm, are cumulatively less than 1%. The dominant constituent of the CDW mineralogy is calcite (55.8%), mainly due to the use of calcium carbonate aggregates in the parent concrete. However, by applying a bimodal crystallite size model for calcite, as described by Bisciotti et al. [69], it was possible to directly estimate the carbonated LCP fraction, which is approximately 10%.

After thermal reactivation at T1, the amorphous content increased, consistent with observations for all HCPs studied. Since AFt and AFm are negligible, this variation can be mainly attributed to changes within the C–S–H structure. It is proposed that at T1, dehydroxylation of C–S–H leads to significant structural modifications, including collapse and disordering of interlayer and semi-crystalline domains, as previously observed in other studies ([50]; Q. [64]; Q. [70]). No notable variations are observed for C_2S or other active mineral phases. At T2, the CDW mineralogy evolved into a more reactive state. The α- and β-C2S fractions increased to 3.6% and 3.0%, respectively, with an additional 0.4% of γ-C2S reported. This process coincided with a reduction in the amorphous content to 19.25%, likely due to crystallization originating from the collapsed C–S–H structure. Interestingly, the calcite content remained stable at 58.8%, with only a slight decrease in the carbonated fraction (5.1%). Comparing the total calcite content at T amb. (65.6%) and T2 (64.0%) confirms that no significant decarbonation occurred.

4.2. Thermogravimetric analyses

The TGA-DTA analyses provide valuable insights into the evolution of the studied samples over the range of 0–900 °C under a controlled atmosphere. The TGA results reflect moisture content, oxidation, decomposition, and thermal stability of the materials during heating. Whereas DTA highlights endothermic and exothermic processes, such as melting, crystallization, or phase transitions. TGA-DTA data measurements were quantified across four key temperature intervals: 50–100 °C, 160–350 °C, 470–650 °C, and 690–900 °C. The full dataset is available in Supplementary Table II.

4.2.1. TGA analyses

The initial weight loss (50–100 °C) corresponds primarily to the evaporation of free and physically bound water, including moisture in the capillary pores and surface water adsorbed, especially for HCPs. The mass loss here is minimal for the CDW sample (−0.67%), indicating limited free or physically bound water. In contrast, the HCP samples show higher values, ranging from −6.84% to −8.46%, except for HCP II, which exhibits a lower loss (−3.15%).

In the next range, the 160–350 °C interval (Fig. 8), closing the T1 threshold, the mass loss is yet associated with water evaporation, in this range previously associated with chemically bonded water [71]. This process corresponds to the decomposition of hydration products, such as AFt and AFm, which are confirmed to disappear at T1 from the XRPD. The CDW again shows the lowest mass loss (−1.73%), while HCPs display higher values. HCP III records the greatest loss (−14.19%), followed by HCP IV (−13.03%) and HCP I (−12.83%) and HCP II (−8.94%). The discrepancy from the XRPD data for the AFt and AFm (0–3.5%) to the TGA data (8.94–14.19%) can be explained from XRPD data by the variation on the amorphous content (5–6%) associated with the C-S-H structure dehydroxylation and collapse ([50]; Y. [51]).

In the 470–650 °C range (Fig. 8), by the T2 threshold, the dehydroxylation of portlandite mainly occurs. The HCP I undergoes the largest mass loss (−6.39%), followed by HCP II (−5.05%). HCP III and IV show more modest losses (−3.99% and −4.27%, respectively), while CDW again exhibits the lowest change (−1.65%). The data follows again the XRPD values for CH (Table I, Supplementary), where HCP I has ~10%, HCP II ~7%, HCP III ~3%, HCP IV ~4%. The remaining difference between the TGA and XRPD values shall be attributed to the complete C-S-H decomposition, described in the literature with decreasing interlayer distance, full

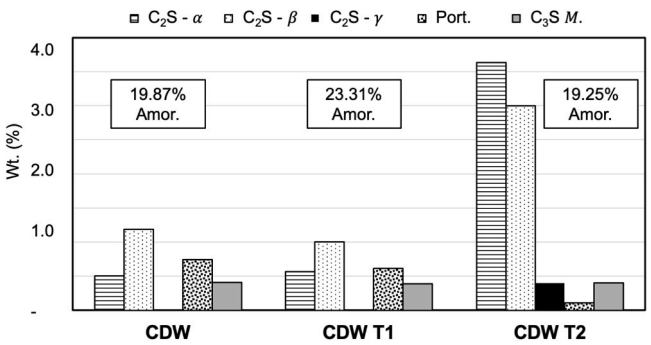

Fig. 7. Bar chart of the QPA results for selected clinker minerals in CDW samples.

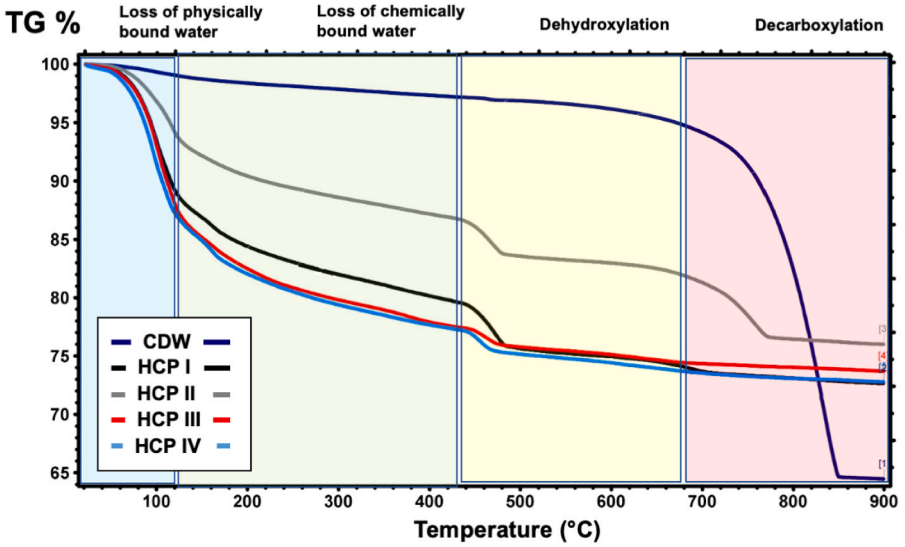

Fig. 8. TGA analyses plot for the HCPs and CDW samples in the range 0–900°C.

structural disordering, and lastly with the complete dissociation of the C-S-H gel [72,73].

Finally, in the high-temperature interval (Fig. 8), beyond T2 (690–900 °C), the decarboxylation of carbonates is observed, including calcite, aragonite, and dolomite if present [38]. The reaction involves CO_2-releasing transformations, and therefore this temperature range shall be avoided. In agreement with the carbonates content from XRPD (Table I, Supplementary), the CDW displays the most significant mass loss (−31.48%), due to its high carbonate content. HCP II follows with a substantial loss of −6.86%, again associated with its SCM limestone filler. The remaining HCPs show only minor decarbonation losses, ranging from −1.28% to −2.20%.

4.2.2. DTA analyses

DTA primarily identifies thermal events occurring in the range 0–900°C. The peak area in DTA curves is roughly proportional to the enthalpy change, although the relationship depends on many factors (packing, heating rate, thermal contact with the reference, furnace design).

The first observable reaction is related to the evaporation of the physically bonded water around 100°C, observed in all the samples studied, although with different magnitudes. The reaction is stronger for HCP I and III, followed by HCP II and IV whereas is negligible for the CDW (Fig. 10). The second peak represents the dehydroxylation of portlandite (CH) in the range of 450°C to 500°C (Fig. 10). The loss shall also correspond, as indicated by previous studies, to the conversion of CH into calcium oxide (CaO) and water [52,53].

The intensity of the transformation agrees with the TGA data, with the HCP I followed by HCP II, III and IV, as also supported by the

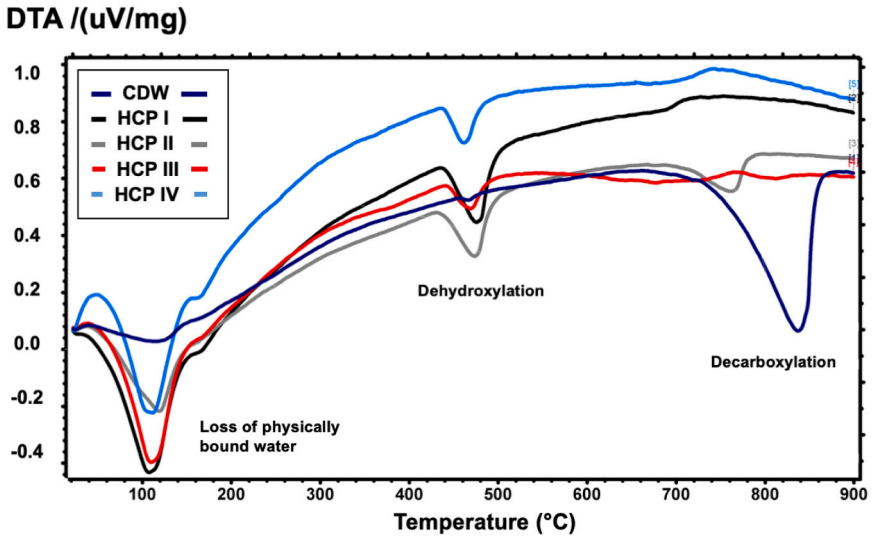

Fig. 9. DTA analyses plot for the HCPs and CDW samples in the range 0–900°C.

XRPD analyses (Table I, Supplementary). The crystallization of the C_2S polymorphs, confirmed by the XRPD data (Figs. 3 and 5), should occur somewhere within the 400–600°C range. Nevertheless, the transition which should be characterized by an exothermic reaction is not observable by the DTA. Neither previous study that employed DSC could observe it [53]. The third endothermic peak appears between 700 °C - 800 °C (Fig. 9), especially for HCP II and CDW, and is associated with the decarboxylation of carbonates. The intensities observed match with the quantitative data from TGA and the XRPD.

4.3. Scanning Electron Microscopy

The SEM analyses highlight morphological and compositional features of the HCPs and of CDW samples at the T amb., T1 and T2 intervals at various magnification scales using either secondary (SE) or backscattered (BSE) electrons.

At T amb., both the HCP and CDW samples consist of a mixture of fine powder and micrograins, with sizes ranging from 10 to 400 μm. In the reference HCP I sample, the grains display predominantly rectangular or angular morphologies, characteristic of shredding and comminution processes (Fig. 10**a**). These grains are mainly composed of a porous matrix, accompanied by fine portlandite crystals and residual clinker minerals such as C_3S present on the surface (Fig. 10**b**).

The CDW have a finer powder content, with limited micrograins, due to the comminution of concrete blocks, where embedded sand is mostly liberated. The bigger grains in this case largely derive again from NAs, appearing primarily as spherical clasts (Fig. 10**c**). The leftover cement grains identified are very few compared to the HCP sample (Fig. 10**d**), their distribution is limited and a reduced presence of CH crystals and residual clinker minerals on their surfaces is found, probably due to carbonation occurring during environmental ageing.

The HCPs and CDW samples have been also embedded in epoxy resin and polished to conduct superficial chemical mapping through BSE. The compositions of HCP I and HCP III at T amb. are displayed in color coding based on their main chemical constituents (Figs. 11**a** and 11**b**). The HCPs are composed of a compact calcium-silicate matrix, primarily made of C-S-H, C-(A)-S-H, and of other hydration products. Other than hydrated compounds the presence of residual anhydrous clinker minerals can be distinguished within the matrix, based on crystal morphologies and chemical point analyses. The C_3S grains (around 20 μm and with Ca/Si ratio close to 3) are typically rectangular in shape, whereas the C_2S are more spherical, have a Ca/Si ratio close to 2, are often assembled in nests, and present a smaller crystal size (around 5 μm). In the case of HCP III, the presence of GGBFS powder can be also seen as tiny Fe, Mg dots scattered in the matrix (Fig. 11**b**). The aluminates minerals (mainly C_3A and C_4AF) are not visible.

After thermal activation at T2, the morphology and crystal assemblage of the HCP samples undergo significant changes (Figs. 11**c**, 11**d**). The calcium–silicate matrix (C–S–H, C–(A)–S–H) is markedly reduced, while abundant C_2S crystal nests develop, separated by an aluminate glassy layer (e.g., C_3A) that forms a distinct rim. The morphology of the C_2S crystals differs between HCP I T2 and HCP III T2: in the former, they appear more regular and spherical, whereas in the latter they are elongated. This variation likely reflects the occurrence of different polymorphs, as confirmed by XRPD analysis (Figs. 3 and 5). Specifically, γ-C_2S predominates in HCP I, while α- and β-C_2S are characteristic of HCP III.

The chemical mapping of the CDW sample at T amb. (Fig. 12**a**) was carried out on a ~400 μm grain of finely crushed concrete (highlighted in red). Residual cement appears as a lighter bluish halo surrounding numerous small clasts (ranging from 50 μm down to just a few μm), of fine sand and micro aggregates. Most of these clasts are calcium carbonate fragments, while others display a siliceous–sodic–ferrous composition, likely corresponding to feldspars. Quartz grains are represented by the clasts with high silicon content (green fragments in Fig. 12**a**).

Comparing the HCP samples at T amb. with the CDW sample at T amb. (Fig. 12**a**) it can be seen how the cement matrix of the latter is more porous and looser than the first one. After the thermal activation at T2 most of the dense leftover cement matrix is not visible anymore, the NAs are liberated and the content of fine powder increases (Fig. 12**b**). At the same time, the thermal reactivation of fine grains still occurred, and the same pattern observed in HCPs for the formation of C_2S nests in spherical grains is observed (Fig. 12**c**). The morphology of the newly formed agglomerate resembles that of clinker nodules (Fig. 12**d**), although a clinkerization process did not occur.

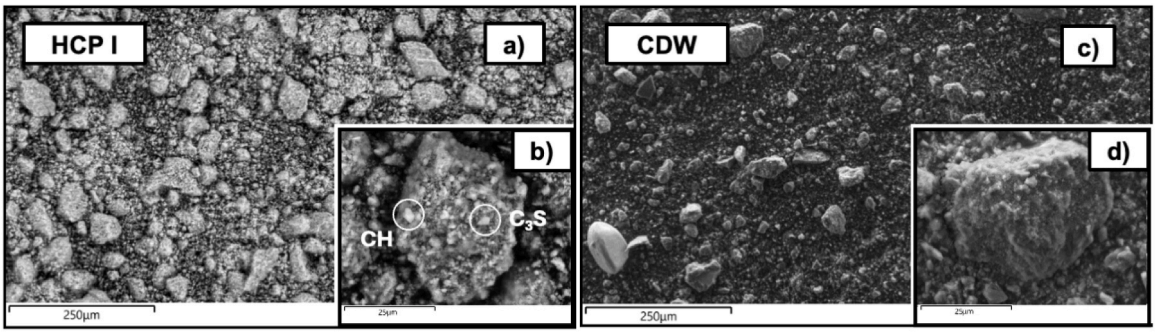

Fig. 10. Scanning Electron Secondary Electron images of HCP and CDW samples.

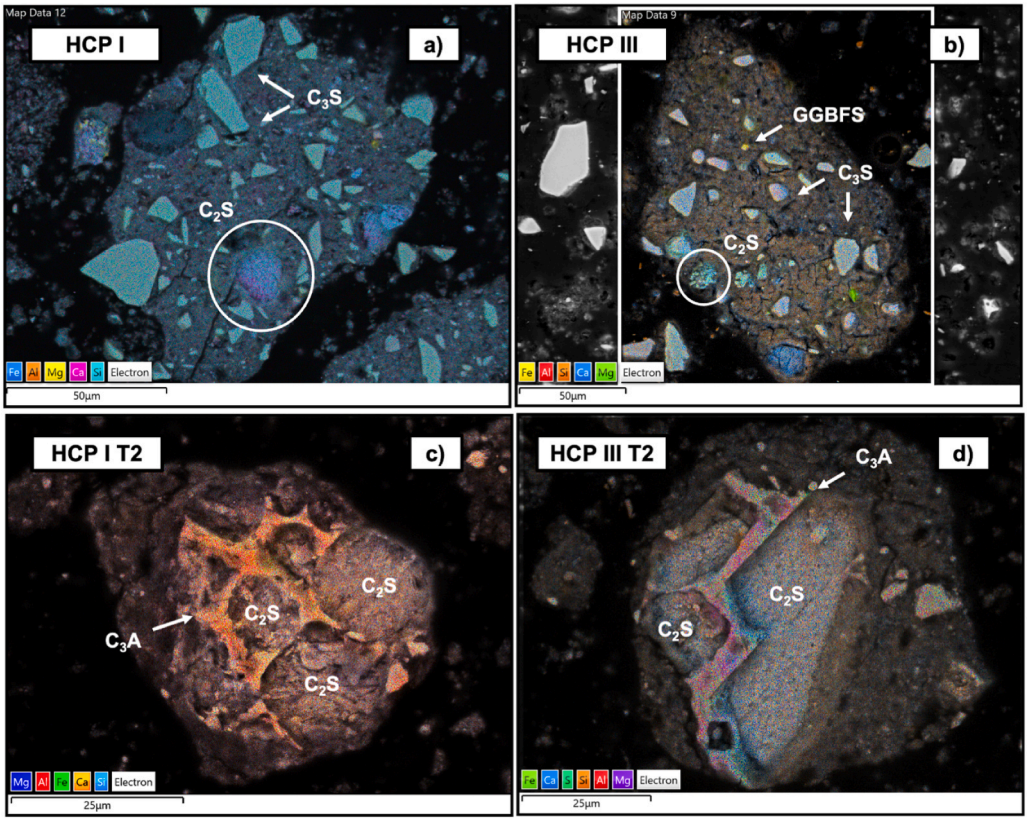

Fig. 11. Scanning Electron Backscattered Electron images of HCP I and HCP III at T amb. and T2.

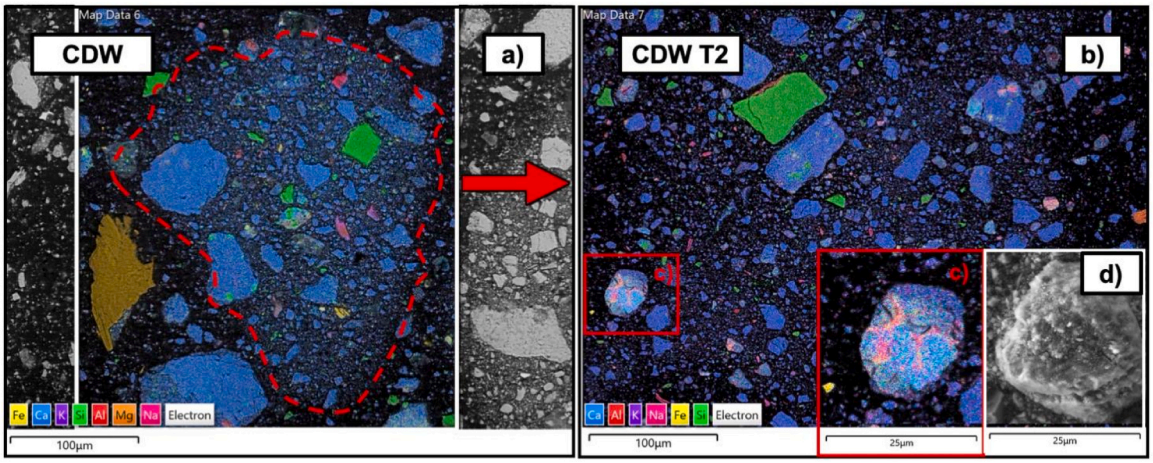

Fig. 12. Scanning Electron Backscattered Electron images of CDW at T amb. and T2.

4.3.1. Reactivity as SCM

The results obtained show the impact on the reactivity of the samples from the thermal activation going from T amb. to T1 and T2, both after 3 and 7 days (Fig. 13). The effectiveness of thermal activation is evidenced from the results by the increasing trend for cumulative heat (J/g) observed for all the HCPs and CDW, when heating from T amb. to T1, and subsequently to T2 (Fig. 13).

In the first step (T amb.–T1), a marked rise is recorded after 3 days, with HCP I, displaying the highest cumulative reactivity increase of + 184%, followed by HCP IV (+141%) and then by the other HCPs samples, while CDW registers a more modest + 46%. A similar pattern is observed after 7 days (Fig. 13). In the second heating step (T1 – T2) the impact on the reactivity from the last heating step is more modest. The highest transition is reported here for HCP IV (+60%) followed by HCP I (+31.3%) and then by the other

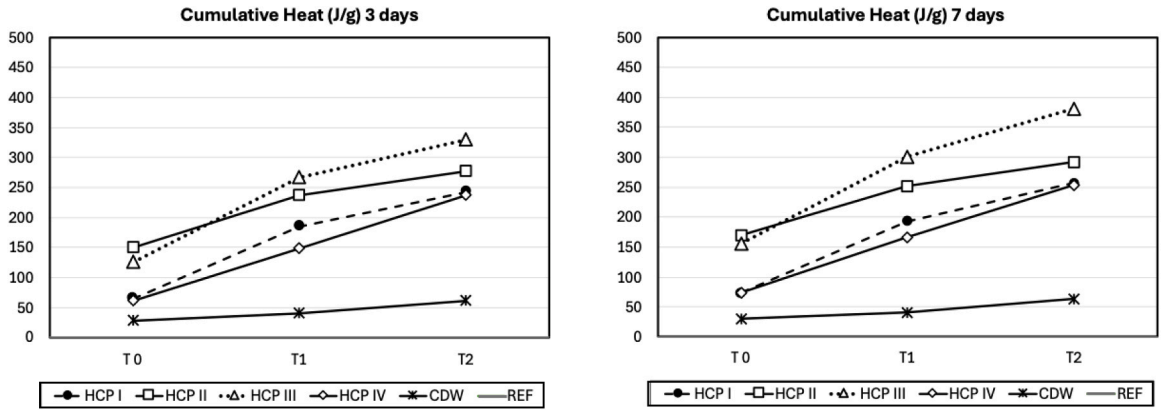

Fig. 13. Cumulative heat (J/g) released by the samples as determined by ASTM C1897–20 method.

samples. In this case, the T2 thermal activation step is considerably more effective for CDW with an increase of + 51%. When it comes to the absolute values the scenario differs. The HCPs samples with the highest reactivity as SCMs, both after T1 and T2, and after 3 and 7 days are the opposite of those reporting the highest cumulative heat increase. These are HCP II and HCP III, with the latter surpassing the first after T1, both at 3 and 7 days. The values measured, respectively 236.3 J/g and 267.4 J/g are five times higher than that for CDW. At T2 the same samples reach 276.7 and 328.9 J/g, where the reference (REF OPC CEM I 52. 5 N) is fixed at 460.7 J/g. At T2, all the HCPs converge within the range of 250–350 J/g, whereas CDW remains consistently lower, around 50 J/g.

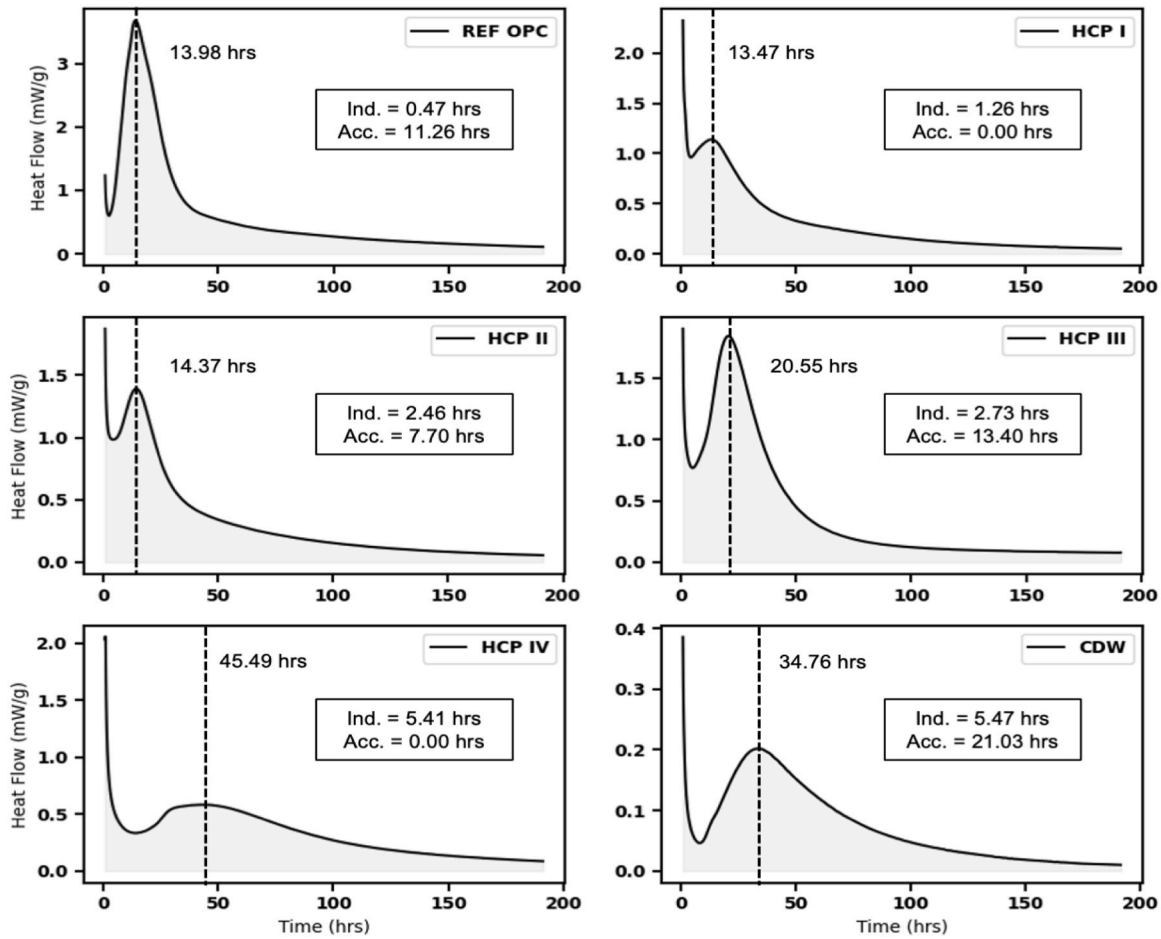

Fig. 14. Diagrams of heat flow over time (hours) for heat of hydration.

4.3.2. Heat of Hydration

Since thermal reactions and the formation of active clinker minerals were mainly observed from XRPD in the T2 samples (Fig. 14), only these are analyzed and described in detail here, while a general discussion of the T1 and T amb. samples is provided in the next section (4.5.1).

The numerical first derivative of heat flow is calculated as:

$$s(t) = \frac{\partial Q}{\partial t} \tag{3}$$

Where Q is the heat flow and t is the time (h).

The beginning of the induction period (I_i) was defined as the earliest time after the initial exotherm when the slope of the heat-flow curve decreased below a small threshold and remained stable for a short persistence interval. The slope threshold (s_i) was set at 5% of the maximum value of $s(t)$ during the first exotherm, and the induction period was considered to start when $s(t)$ exceeded this threshold. The maximum heat-flow peak (P_M), corresponding to the acceleration stage, was then identified as the highest recorded heat flow (mW/g).

Between I_i and P_M, the maximum slope was determined, and a second threshold (S_f) was defined as 5% of this value. The end of the induction period was assigned to the time when $s(t)$ fell below S_f. The mean heat flow during the induction period ($\bar{I}$) was also calculated together with its 5% threshold, and the onset of the acceleration stage was defined as the time when $s(t)$ exceeded this threshold. The acceleration stage ends at P_M, and the mean heat release during this stage was denoted as P^{-}. The 5% threshold was selected as a conservative criterion, ensuring that only the most distinct occurrences of the hydration stages are identified.

A qualitative comparison highlights that the first clear difference between the reference OPC and the HCPs lies in the heat generated during the initial exotherm, which reflects the presence of CH. These results are consistent with the XRPD quantitative analysis of CH (Fig. 3). A second difference concerns the time required to reach P_M, which is similar for OPC, HCP I, and HCP II (around 14 h), but significantly longer for HCP III, HCP IV, and CDW (Fig. 14).

When considering the quantitative data, a more detailed interpretation can be provided. The induction period, or dormant stage, is governed by a series of physico-chemical mechanisms that temporarily reduce dissolution and precipitation rates. The primary factor regulating this process is the saturation of the pore solution with Ca^{2+}, OH^{-}, and SO_4^{2-} ions. The induction period concludes once stable nuclei of C–S–H and portlandite begin to form and grow rapidly, thereby initiating the acceleration stage. As shown in Fig. 14 and Table 4, this transition occurs much earlier in OPC (0.47 h), while it is noticeably prolonged in all HCPs. The incorporation of SCMs further extends the induction period, ranging from 1.26 to 5.41 h, with the maximum value recorded for CDW (5.47 h). The mean heat release ($\bar{I}$), although comparable, is consistently higher in HCPs than in the reference OPC, whereas it remains very modest in CDW. This behavior can be attributed to the residual presence of CH in the HCP samples (Fig. 4), which promotes solution saturation and consequently delays the nucleation and growth of C–S–H and portlandite.

The acceleration stage corresponds to the dissolution of C_3S and C_2S crystals and represents the main kinetic phase of cement hydration. In the reference OPC, this stage lasts 11.26 h, with an average heat release of 2.18 mW/g (Table 4). The behavior of the HCPs, however, differs significantly. HCP I and HCP IV do not exhibit any detectable acceleration stage based on the calculations (based on the conservative 5% threshold), while CDW, although assigned one, shows only a very weak response. A distinct condition is observed in HCP II and HCP III, where the acceleration stage extends for 7.70 and 13.40 h, respectively, with corresponding average heat releases of 1.22 and 1.34 mW/g (Table 4).

This evidence is consistent with the cumulative heat release of the hydration process (ΣH), measured at 3 and 7 days. As shown in Table 4, the HCPs that exhibited little or no acceleration stage, namely HCP I and HCP IV, also recorded the lowest ΣH values. When compared with the reference OPC (404.10 J/g at 7 days), it is noteworthy that HCP III achieved the highest ΣH among the blended systems (260.40 J/g at 7 days), followed by HCP II and HCP IV, with 211.32 and 209.30 J/g at 7 days, respectively. The full dataset is provided in Table IV of Supplementary.

5. The influence of mineralogy on thermal reactivation of CDW

The starting composition of the HCPs and of the CDW depends strongly on the original type of cement used (as classified by EN 197–1), SCM type and presence, and ageing occurred (carbonation). In the case of CDW the type of NAs (natural aggregates) and quantity embedded, also plays a crucial role. After thermal reactivation, based on these conditions a different final product is obtained, with variable hydraulic and pozzolanic (SCM) reactivity.

- At **T amb. (25 °C):** The materials are mainly composed of an amorphous phase, the majority of which is C-S-H, C-A-H, or C-(A-)S-H. In a standard HCP I, this fraction accounts for about 70% of the total, increasing to 80% in HCP III (due to GGBFS presence) and decreasing to 60% in HCP II (with limestone). Residual anhydrous clinker minerals are negligible at this stage in terms of hydraulic or SCM reactivity. However, for HCP II and HCP III, the embedded limestone and GGBFS already provide significant SCM reactivity (150 and 125 J/g, respectively).
- At **T1 (350 °C):** The amorphous content increases substantially, mainly due to the decomposition of hydrated phases and the collapse of semi-crystalline C-S-H interlayers into amorphous SiO_2 and Al_2O_3. Residual anhydrous clinker minerals remain negligible from a hydraulic perspective, but the SCM reactivity increases in all systems, owing to amorphization, in the range between + 50% and + 200%, compared to T amb.

Table 4
Cumulative heat release (ΣH) at 3 and 7 days, mean heat during induction ($\bar{I}$) and mean heat during acceleration ($\bar{P}$).

Sample	$\bar{I}$ *(mW/g)*	$\bar{P}$ (mW/g)	*ΣH at 3 dd (J/g)*	*ΣH at 7 dd (J/g)*
OPC REF	0.6	2.2	324.6	404.1
HCP I T2	0.9	-	157.4	199.7
HCP II T2	1.0	1.2	167.1	211.3
HCP III T2	0.8	1.3	221.5	260.4
HCP IV T2	0.4	-	132.5	209.3
CDW T2	0.1	0.1	35.0	48.0

- At **T2 (600 °C):** The amorphous fraction sharply decreases across all samples due to crystallization of C_2S polymorphs (α, β, and γ). In HCP I, γ-C_2S is the predominant phase, while in the blended systems (HCP II, III, and IV), its formation is restricted or entirely suppressed, likely due to impurities from the supplementary materials (GGBFS, limestone, and pozzolans) causing ionic substitution that blocks the phase-transition. Instead, α′H-C_2S (6–10%) is predominant, with β-C_2S also present (4–7%). Hydraulic reactivity correlates with the combined α′H and β content, except in HCP III, where its high amorphous fraction appears to hinder effective QPA of C_2S polymorphs. Empirical data (Table 4) show HCP III to be the most effective hydraulic binder at this stage, achieving a hydration heat of 221 J/g, comparable to standard OPC CEM I 52.5 N (323 J/g). Additionally, at this under-calcining temperature, no decomposition of $CaCO_3$ into CO_2 is observed.
- For CDW, the key parameter of interest is the proportion of HCP or LCP. In the analyzed samples from a recycling facility, this fraction represents approximately 27% of the total, originally produced with CEM I 52.5 N (EN 197–1), corresponding to HCP I. In a hypothetical scenario where the LCP fraction reaches nearly 100%, the material would exhibit behavior comparable to HCP I. However, due to the calcite enrichment typically observed in CDW, its composition more closely resembles that of HCP II, which contains limestone and has demonstrated enhanced reactivity compared to HCP I. Therefore, if CDW is ground to a filler-sized fraction prior to thermal reactivation, the ideal scenario with 100% LCP could achieve performance similar to HCP II, which has shown better SCM reactivity compared to HCP I. The most promising case, however, is represented by CDW originating from GGBFS-blended cement (HCP III), which exhibits the highest reactivation potential after recycling. With 100% LCP, its performance approaches that of standard OPC 52.5 N after T2 (600 °C), without inducing $CaCO_3$ decomposition into CO_2.
- Finally, we confirm that at the T2 under-calcining temperature adopted (600 °C), the formation of C_2S-γ is favored. Although this polymorph is less reactive than the other C_2S phases, previous literature reported its potential in CO_2 mineralization and carbon uptake [74,75].

6. Conclusions

Thermal activation efficiency of hydrated cement pastes (HCPs) and construction and demolition waste (CDW) is strongly governed by the original cement composition, including cement type, SCM incorporation, and aggregate content:

1. Thermal treatment at 350 °C primarily promotes amorphization, which enhances the reactivity of SCM-rich systems and favors pozzolanic activity.
2. At 600 °C, the hydraulic behavior is mainly controlled by the crystallization of C_2S polymorphs, indicating a shift from amorphous-driven to phase-controlled reactivity.
3. GGBFS-blended cement (HCP III) exhibited the highest reactivation potential among the investigated systems, achieving mechanical performance comparable to CEM I 52.5 N without inducing $CaCO_3$ decomposition.
4. For CDW-derived materials, reactivity is closely linked to the relative content of HCP/LCP, with GGBFS-based waste again emerging as the most promising precursor.
5. The dominance of γ-C_2S at 600 °C, despite its intrinsically low hydraulic activity, highlights the potential of coupling thermal reactivation with enforced carbonation to enhance pozzolanic behavior while simultaneously enabling CO_2 mineralization.

Based on these results, further studies are required to investigate the properties of CDW treated at 600 °C and subjected to enforced carbonation of the formed γ-C_2S. The pozzolanic behavior of the resulting material may lead to the development of a highly reactive, carbon-negative supplementary cementitious material (SCM).

CRediT authorship contribution statement

A. Bisciotti: Conceptualization, Methodology, Validation, Formal analysis, Investigation, Visualization, Writing – original draft, Project administration. **S. Castellini:** Methodology, Validation, Formal analysis, Investigation, Data curation, Writing – original draft. **A. Neri:** Conceptualization, Methodology, Validation, Supervision, Writing – review & editing. **P. Šajna:** Formal analysis, Validation, Software, Data curation. **S. Dolenec:** Methodology, Validation, Writing – original draft. **A. Balbo:** Methodology, Validation, Funding acquisition. **G. Cruciani:** Conceptualization, Writing – review & editing, Supervision, Funding acquisition.

Funding

The project was financial supported under the National Recovery and Resilience Plan (NRRP), Mission 4, Component 2, Investment 1.1, Call for tender No. 104 published on 2.2.2022 by the Italian Ministry of University and Research (MUR), funded by the European Union – NextGenerationEU – Project Title "Rubble-to-Resource (RUB2RES): Earth science knowledge for sorting and recycling Construction and Demolition Waste" – CUP F53D23002140006 - Grant Assignment Decree No. 965 adopted on 30.06.2023.

Declaration of Competing Interest

The authors declare that they have no known competing financial interests or personal relationships that could have appeared to influence the work reported in this paper.

Acknowledgments

The authors gratefully acknowledge Michele Capoccia of the Colacem Spa laboratory for his assistance in preparing the mortar samples. We also extend our thanks to Dr. Fabio Santinelli from Colacem Spa's R&D department for his valuable insights and support throughout this research.

Appendix A. Supporting information

Supplementary data associated with this article can be found in the online version at doi:10.1016/j.cscm.2026.e05978.

References

[1] M.C.G. Juenger, R. Snellings, S.A. Bernal, Supplementary cementitious materials: New sources, characterization, and performance insights, in: Cement and Concrete Research, 122, Elsevier Ltd, 2019, pp. 257–273, https://doi.org/10.1016/j.cemconres.2019.05.008.
[2] S. Kumar, A. Gangotra, M. Barnard, Towards a net zero cement: strategic policies and systems thinking for a low-carbon future, Curr. Sustain. Renew. Energy Rep. 12 (1) (2025) 5, https://doi.org/10.1007/s40518-025-00253-0.
[3] M. Juenger, J.L. Provis, J. Elsen, W. Matthes, R.D. Hooton, J. Duchesne, L. Courard, H. He, F. Michel, R. Snellings, N. De Belie, Supplementary cementitious materials for concrete: characterization needs, Mater. Res. Soc. Symp. Proc. (2012) *1488*, https://doi.org/10.1557/opl.2012.
[4] L. Brinkman, S.A. Miller, Environmental impacts and environmental justice implications of supplementary cementitious materials for use in concrete, Environ. Res. Infrastruct. Sustain. 1 (2) (2021), https://doi.org/10.1088/2634-4505/ac0e86.
[5] M. Frías, S. Martínez-Ramírez, R.V. de la Villa, L. Fernández-Carrasco, R. García, Reactivity in cement pastes bearing fine fraction concrete and glass from construction and demolition waste: Microstructural analysis of viability, Cem. Concr. Res. 148 (2021), https://doi.org/10.1016/j.cemconres.2021.106531.
[6] X. Jiang, R. Xiao, Y. Bai, B. Huang, Y. Ma, Influence of waste glass powder as a supplementary cementitious material (SCM) on physical and mechanical properties of cement paste under high temperatures, J. Clean. Prod. 340 (2022) 130778, https://doi.org/10.1016/j.jclepro.2022.130778.
[7] S. Barbhuiya, F. Kanavaris, B.B. Das, M. Idrees, Decarbonising cement and concrete production: Strategies, challenges and pathways for sustainable development, J. Build. Eng. 86 (2024) 108861, https://doi.org/10.1016/j.jobe.2024.108861.
[8] D.O. de Lima, D.S. de Lira, M.F. Rojas, H.S. Junior, Assessment of the potential use of construction and demolition waste (CDW) fines as eco-pozzolan in binary and ternary cements, Constr. Build. Mater. 411 (2024), https://doi.org/10.1016/j.conbuildmat.2023.134320.
[9] Z. Abedin Khan, U. Balunaini, S. Costa, N.H.T. Nguyen, A review on sustainable use of recycled construction and demolition waste aggregates in pavement base and subbase layers, Clean. Mater. 13 (2024) 100266, https://doi.org/10.1016/j.clema.2024.100266.
[10] T.F. Baggio, E. Possan, J.J. de Oliveira Andrade, Physical-chemical characterization of construction and demolition waste powder with thermomechanical activation for use as supplementary cementitious material, Constr. Build. Mater. 437 (2024), https://doi.org/10.1016/j.conbuildmat.2024.136907.
[11] Z. Ma, J. Shen, C. Wang, H. Wu, Characterization of sustainable mortar containing high-quality recycled manufactured sand crushed from recycled coarse aggregate, Cem. Concr. Compos. 132 (2022) 104629, https://doi.org/10.1016/j.cemconcomp.2022.104629.
[12] Z. Ma, Y. Wu, B. Wang, C. Liang, Y. Zhang, C. Wang, Understanding the micro-characteristics and mechanical behavior of more sustainable UHP-ECC with both recycled aggregate and recycled powder from concrete waste, J. Build. Eng. 112 (2025) 113705, https://doi.org/10.1016/j.jobe.2025.113705.
[13] Y. Chen, B. Zhan, L. Hong, B. Guo, P. bian, C. Wang, X. Hong, Q. Yu, A new perspective on the effect of residual paste content on the properties of recycled fine aggregates, J. Build. Eng. 94 (2024) 110070, https://doi.org/10.1016/j.jobe.2024.110070.
[14] S. Hossenejad, S. Hamidi, M. Ghassemieh, Numerical investigation of the seismic performance of a self-centering steel frame with SMA-based dampers. Journal of Building Engineering, J. Build. Eng. 76 (2023) 107321, https://doi.org/10.1016/j.jobe.2023.107321.
[15] A. Bisciotti, L. Mancini, A. Viani, V.Z. Serjun, A. Mladenovic, G. Cruciani, Multi-scale X-ray techniques for assessing recycled concrete aggregate: from XRPD analysis of leftover cement in recycled aggregates to micro-CT imaging of concrete microstructure, Dev. Built Environ. 23 (2025) 100709, https://doi.org/10.1016/j.dibe.2025.100709.
[16] M. Cisiński, G. Biava, F. Winnefeld, Ł. Sadowski, M. Ben Haha, M. Zajac, Carbonated calcium silicates as pozzolanic supplementary cementitious materials, Constr. Build. Mater. 443 (2024) 137764, https://doi.org/10.1016/j.conbuildmat.2024.137764.
[17] M. Zajac, I. Maruyama, A. Iizuka, J. Skibsted, Enforced carbonation of cementitious materials, Cem. Concr. Res. 174 (2023), https://doi.org/10.1016/j.cemconres.2023.107285.
[18] M. Zajac, J. Skocek, Ł. Gołek, J. Deja, Supplementary cementitious materials based on recycled concrete paste, J. Clean. Prod. 387 (2023), https://doi.org/10.1016/j.jclepro.2022.135743.
[19] S. Maruthupandian, A. Chrysanthou, A. Kanellopoulos, Assessing the upcycling potential of construction and demolition waste derived silt: Activation, physicochemical and mineralogical characterisation, Constr. Build. Mater. 493 (2025) 143163, https://doi.org/10.1016/j.conbuildmat.2025.143163.
[20] D. Zhang, S. Zhang, B. Huang, Q. Yang, J. Li, Comparison of mechanical, chemical, and thermal activation methods on the utilisation of recycled concrete powder from construction and demolition waste, J. Build. Eng. 61 (2022) 105295, https://doi.org/10.1016/j.jobe.2022.105295.
[21] A. Carriço, J.A. Bogas, M. Guedes, Thermoactivated cementitious materials – A review, Constr. Build. Mater. 250 (2020) 118873, https://doi.org/10.1016/j.conbuildmat.2020.118873.
[22] H. Wu, J. Xu, D. Yang, Z. Ma, Utilizing thermal activation treatment to improve the properties of waste cementitious powder and its newmade cementitious materials, J. Clean. Prod. 322 (2021) 129074, https://doi.org/10.1016/j.jclepro.2021.129074.

[23] W. Kurdowski, Portland Cement Clinker, in: W. Kurdowski (Ed.), Cement and Concrete Chemistry, Springer Netherlands, 2014, pp. 21–127, https://doi.org/10.1007/978-94-007-7945-7_2.

[24] A. Tokareva, S. Kaassamani, D. Waldmann, Fine demolition wastes as Supplementary cementitious materials for CO2 reduced cement production, Constr. Build. Mater. 392 (2023), https://doi.org/10.1016/j.conbuildmat.2023.131991.

[25] S. Zhutovsky, A. Shishkin, Recycling of hydrated Portland cement paste into new clinker, Constr. Build. Mater. 280 (2021), https://doi.org/10.1016/j.conbuildmat.2021.122510.

[26] R. Serpell, M. Lopez, Properties of mortars produced with reactivated cementitious materials, Cem. Concr. Compos. 64 (2015) 16–26, https://doi.org/10.1016/j.cemconcomp.2015.08.003.

[27] R. Serpell, F. Zunino, Recycling of hydrated cement pastes by synthesis of α′H-C2S, Cem. Concr. Res. 100 (2017) 398–412, https://doi.org/10.1016/j.cemconres.2017.08.001.

[28] S. Real, A. Carriço, J.A. Bogas, M. Guedes, Influence of the Treatment Temperature on the Microstructure and Hydration Behavior of Thermoactivated Recycled Cement, Materials 13 (18) (2020), https://doi.org/10.3390/ma13183937.

[29] A. Gholizadeh-Vayghan, G. Meza Hernandez, F.K. Kingne, J. Gu, N. Dilissen, M. El Kadi, T. Tysmans, J. Vleugels, H. Rahier, R. Snellings, Thermal Reactivation of Hydrated Cement Paste: Properties and Impact on Cement Hydration, Materials 17 (11) (2024), https://doi.org/10.3390/ma17112659.

[30] J. Dweck, M.B.M. Melchert, F.K. Cartledge, R.S. Leonardo, R.D. Toledo Filho, A comparative study of hydration kinetics of different cements by thermogravimetry on calcined mass basis, J. Therm. Anal. Calorim. 128 (3) (2017) 1335–1342, https://doi.org/10.1007/s10973-016-6080-8.

[31] B. Pacewska, M. Nowacka, Studies of conversion progress of calcium aluminate cement hydrates by thermal analysis method, J. Therm. Anal. Calorim. 117 (2) (2014) 653–660, https://doi.org/10.1007/s10973-014-3804-5.

[32] R. Snellings, P. Suraneni, J. Skibsted, Future and emerging supplementary cementitious materials, Cem. Concr. Res. 171 (2023), https://doi.org/10.1016/j.cemconres.2023.107199.

[33] I.G. Richardson, Tobermorite/jennite- and tobermorite/calcium hydroxide-based models for the structure of C-S-H: Applicability to hardened pastes of tricalcium silicate, β-dicalcium silicate, Portland cement, and blends of Portland cement with blast-furnace slag, metakaolin, or silica fume, Cem. Concr. Res. 34 (9) (2004) 1733–1777, https://doi.org/10.1016/j.cemconres.2004.05.034.

[34] X. Zhu, I.G. Richardson, Morphology-structural change of C-A-S-H gel in blended cements, Cem. Concr. Res. 168 (2023), https://doi.org/10.1016/j.cemconres.2023.107156.

[35] J. Li, W. Zhang, P.J.M. Monteiro, Synchrotron X-ray Raman scattering shows the changes of the Ca environment in C-S-H exposed to high pressure, Cem. Concr. Res. 132 (2020), https://doi.org/10.1016/j.cemconres.2020.106066.

[36] V.M. Pereira, R. Baldusco, P.B. Silva, V.A. Quarcioni, R.S. Motta, S. Suzuki, S.C. Angulo, Thermoactivated cement from construction and demolition waste for pavement base stabilization: A case study in Brazil, Waste Manag. Res. 43 (1) (2025) 121–132, https://doi.org/10.1177/0734242X241227370.

[37] J. Villar-Hernández, E. Villar-Cociña, H. Savastano, M.F. Rojas, Valorization of Fine-Fraction CDW in Binary Pozzolanic CDW/Bamboo Leaf Ash Mixtures for the Elaboration of New Ternary Low-Carbon Cement, Resources 13 (7) (2024), https://doi.org/10.3390/resources13070100.

[38] I. Galan, F.P. Glasser, C. Andrade, Calcium carbonate decomposition, J. Therm. Anal. Calorim. 111 (2) (2013) 1197–1202, https://doi.org/10.1007/s10973-012-2290-x.

[39] T. Baran, P. Pichniarczyk, Correlation factor between heat of hydration and compressive strength of common cement, Constr. Build. Mater. 150 (2017) 321–332, https://doi.org/10.1016/j.conbuildmat.2017.06.025.

[40] L. Wadsö, M. Arndt, An international round robin test on isothermal (conduction) calorimetry for measurement of three-day heat of hydration of cement, Cem. Concr. Res. 79 (2016) 316–322, https://doi.org/10.1016/j.cemconres.2015.10.004.

[41] F. Avet, R. Snellings, A. Alujas Diaz, M. Ben Haha, K. Scrivener, Development of a new rapid, relevant and reliable (R3) test method to evaluate the pozzolanic reactivity of calcined kaolinitic clays, Cem. Concr. Res. 85 (2016) 1–11, https://doi.org/10.1016/j.cemconres.2016.02.015.

[42] X. Li, R. Snellings, M. Antoni, N.M. Alderete, M. Ben Haha, S. Bishnoi, Ö. Cizer, M. Cyr, K. De Weerdt, Y. Dhandapani, J. Duchesne, J. Haufe, D. Hooton, M. Juenger, S. Kamali-Bernard, S. Kramar, M. Marroccoli, A.M. Joseph, A. Parashar, K.L. Scrivener, Reactivity tests for supplementary cementitious materials: RILEM TC 267-TRM phase 1, Mater. Struct. Mater. Et. Constr. 51 (6) (2018), https://doi.org/10.1617/s11527-018-1269-x.

[43] G. Le Saoût, V. Kocaba, K. Scrivener, Application of the Rietveld method to the analysis of anhydrous cement, in: Cement and Concrete Research, 41, Elsevier Ltd, 2011, pp. 133–148, https://doi.org/10.1016/j.cemconres.2010.10.003.

[44] T. Matschei, B. Lothenbach, F.P. Glasser, The AFm phase in Portland cement, Cem. Concr. Res. 37 (2) (2007) 118–130, https://doi.org/10.1016/j.cemconres.2006.10.010.

[45] S.T. Bergold, F. Goetz-Neunhoeffer, J. Neubauer, Quantitative analysis of C-S-H in hydrating alite pastes by in-situ XRD, Cem. Concr. Res. 53 (2013) 119–126, https://doi.org/10.1016/j.cemconres.2013.06.001.

[46] G. Sun, J. Zhang, N. Yan, Microstructural evolution and characterization of ground granulated blast furnace slag in variant pH, Constr. Build. Mater. 251 (2020) 118978, https://doi.org/10.1016/j.conbuildmat.2020.118978.

[47] G. Habert, N. Choupay, J.M. Montel, D. Guillaume, G. Escadeillas, Effects of the secondary minerals of the natural pozzolans on their pozzolanic activity, Cem. Concr. Res. 38 (7) (2008) 963–975, https://doi.org/10.1016/j.cemconres.2008.02.005.

[48] S. Grangeon, F. Claret, Y. Linard, C. Chiaberge, X-ray diffraction: a powerful tool to probe and understand the structure of nanocrystalline calcium silicate hydrates, Acta Crystallogr. Sect. B 69 (5) (2013) 465–473, https://doi.org/10.1107/S2052519213021155.

[49] H. Suh, H. Jee, J. Kim, R. Kitagaki, S. Ohki, S. Woo, K. Jeong, S. Bae, Influences of rehydration conditions on the mechanical and atomic structural recovery characteristics of Portland cement paste exposed to elevated temperatures, Constr. Build. Mater. 235 (2020) 117453, https://doi.org/10.1016/j.conbuildmat.2019.117453.

[50] J. Yang, W. Zhang, D. Hou, G. Zhang, Q. Ding, Structure, dynamics and mechanical properties evolution of calcium silicate hydrate induced by dehydration and dehydroxylation, Constr. Build. Mater. 291 (2021) 123327, https://doi.org/10.1016/j.conbuildmat.2021.123327.

[51] Y. Zhang, Q. Zhou, J.W. Ju, M. Bauchy, New insights into the mechanism governing the elasticity of calcium silicate hydrate gels exposed to high temperature: A molecular dynamics study, Cem. Concr. Res. 141 (2021) 106333, https://doi.org/10.1016/j.cemconres.2020.106333.

[52] E. Menéndez, C. Andrade, L. Vega, Study of dehydration and rehydration processes of portlandite in mature and young cement pastes, J. Therm. Anal. Calorim. 110 (1) (2012) 443–450, https://doi.org/10.1007/s10973-011-2167-4.

[53] N. Noel, T. Mielke, G. Semugaza, A.Z. Gierth, S. Helmich, S. Nawrath, D.C. Lupascu, Chemical transformations during the preparation and rehydration of reactivated virgin cements, CEMENT 19 (2025) 100129, https://doi.org/10.1016/j.cement.2025.100129.

[54] G. Semugaza, T. Mielke, M.E. Castillo, A.Z. Gierth, J.X. Tam, S. Nawrath, D.C. Lupascu, Reactivation of hydrated cement powder by thermal treatment for partial replacement of ordinary portland cement, Materials and Structures 56 (3) (2023), https://doi.org/10.1617/s11527-023-02133-9.

[55] G. Semugaza, T. Mielke, M.E. Castillo, A.Z. Gierth, J.X. Tam, S. Nawrath, D.C. Lupascu, Reactivation of hydrated cement powder by thermal treatment for partial replacement of ordinary portland cement, Mater. Struct. /Mater. Et. Constr. 56 (3) (2023), https://doi.org/10.1617/s11527-023-02133-9.

[56] A. Gies, D. Knöfel, Influence of alkalies on the composition of belite-rich cement clinkers and the technological properties of the resulting cements, Cem. Concr. Res. 16 (3) (1986) 411–422, https://doi.org/10.1016/0008-8846(86)90117-1.

[57] Y.-M. Kim, S.-H. Hong, Influence of Minor Ions on the Stability and Hydration Rates of β-Dicalcium Silicate, J. Am. Ceram. Soc. 87 (5) (2004) 900–905, https://doi.org/10.1111/j.1551-2916.2004.00900.x.

[58] K. Morsli, Á.G. De La Torre, S. Stöber, A.J.M. Cuberos, M. Zahir, M.A.G. Aranda, Quantitative Phase Analysis of Laboratory-Active Belite Clinkers by Synchrotron Powder Diffraction, J. Am. Ceram. Soc. 90 (10) (2007) 3205–3212, https://doi.org/10.1111/j.1551-2916.2007.01870.x.

[59] A. Elhoweris, I. Galan, F.P. Glasser, Stabilisation of α′ dicalcium silicate in calcium sulfoaluminate clinker, Adv. Cem. Res. 32 (3) (2018) 112–124, https://doi.org/10.1680/jadcr.18.00050.

[60] H. Eckert, S. Divilov, M.J. Mehl, D. Hicks, A.C. Zettel, M. Esters, X. Campilongo, S. Curtarolo, The AFLOW Library of Crystallographic Prototypes: Part 4, Comput. Mater. Sci. 240 (2024) 112988, https://doi.org/10.1016/j.commatsci.2024.112988Focustolearnmore.

[61] S.N. Ghosh, P.B. Rao, A.K. Paul, K. Raina, The chemistry of dicalcium silicate mineral, J. Mater. Sci. 14 (7) (1979) 1554–1566, https://doi.org/10.1007/BF00569274.
[62] S. Shibata, K. Kishi, K. Asaga, M. Daimon, P.R. Shrestha, Preparation and hydration of β-C2S without stabilizer, Cem. Concr. Res. 14 (3) (1984) 323–328, https://doi.org/10.1016/0008-8846(84)90049-8.
[63] F. von Lampe, R. Seydel, On a new form of β-belite, Cem. Concr. Res. 19 (4) (1989) 509–518, https://doi.org/10.1016/0008-8846(89)90002-1.
[64] Q. Zhang, G. Ye, E. Koenders, Investigation of the structure of heated Portland cement paste by using various techniques, Constr. Build. Mater. 38 (2013) 1040–1050, https://doi.org/10.1016/j.conbuildmat.2012.09.071.
[65] Á.G. De la Torre, S. Bruque, J. Campo, M.A.G. Aranda, The superstructure of $C_{3}S$ from synchrotron and neutron powder diffraction and its role in quantitative phase analyses, Cement and Concrete Research 32 (9) (2002) 1347–1356, https://doi.org/10.1016/S0008-8846(02)00810-6.
[66] G. Bonifazi, R. Palmieri, S. Serranti, Evaluation of attached mortar on recycled concrete aggregates by hyperspectral imaging, Constr. Build. Mater. 169 (2018) 835–842, https://doi.org/10.1016/j.conbuildmat.2018.03.048.
[67] S. Braymand, S. Roux, H. Fares, K. Déodonne, F. Feugeas, Separation and Quantification of Attached Mortar in Recycled Concrete Aggregates, Waste Biomass.. Valoriz. 8 (5) (2017) 1393–1407, https://doi.org/10.1007/s12649-016-9771-2.
[68] G. Liu, Q. Li, J. Song, L. Wang, H. Liu, Y. Guo, G. Yue, Quantitative analysis of surface attached mortar for recycled coarse aggregate, Materials 15 (1) (2022), https://doi.org/10.3390/ma15010257.
[69] A. Bisciotti, D. Jiang, Y. Song, G. Cruciani, Estimating attached mortar paste on the surface of recycled aggregates based on deep learning and mineralogical models, Clean. Mater. 11 (2024) 100215, https://doi.org/10.1016/j.clema.2023.100215.
[70] Q. Zhang, G. Ye, Dehydration kinetics of Portland cement paste at high temperature, J. Therm. Anal. Calorim. 110 (1) (2012) 153–158, https://doi.org/10.1007/s10973-012-2303-9.
[71] S. Maheswaran, N.R. Iyer, G.S. Palani, R.A. Pandi, D.D. Dikar, S. Kalaiselvam, Effect of high temperature on the properties of ternary blended cement pastes and mortars, J. Therm. Anal. Calorim. 122 (2) (2015) 775–786, https://doi.org/10.1007/s10973-015-4817-4.
[72] X. Cong, R.J. Kirkpatrick, Effects of the temperature and relative humidity on the structure of C□S□H gel, Cem. Concr. Res. 25 (6) (1995) 1237–1245, https://doi.org/10.1016/0008-8846(95)00116-T.
[73] C.E. White, Effects of temperature on the atomic structure of synthetic calcium–silicate–deuterate gels: A neutron pair distribution function investigation, Cem. Concr. Res. 79 (2016) 93–100, https://doi.org/10.1016/j.cemconres.2015.09.001.
[74] M. Lei, Y. Mu, Z. Liu, F. Wang, S. Hu, Structural Evolution and Characterization of γ-C2S (γ-C2S) Compacts during Carbonation, ACS Sustain. Chem. & Eng. 11 (1) (2023) 444–457, https://doi.org/10.1021/acssuschemeng.2c06623.
[75] L. Yu, B. Lu, J. Sun, R. Jiang, Z. Liu, Z. Zhang, H.M. Naguib, G. Hou, A novel approach to accelerate the carbonation of γ-C2S under atmospheric pressure: Increasing CO2 dissolution and promoting calcium ion leaching via triethanolamine, Constr. Build. Mater. 450 (2024) 138719, https://doi.org/10.1016/j.conbuildmat.2024.138719.